

Catalytic Mechanism of Cofactor-Free Dioxygenases and How They Circumvent Spin-Forbidden Oxygenation of Their Substrates

Aitor Hernández-Ortega,[†] Matthew G. Quesne,[‡] Soi Bui,[§] Derren J. Heyes,[†] Roberto A. Steiner,[§] Nigel S. Scrutton,^{*,†} and Sam P. de Visser^{*,‡}

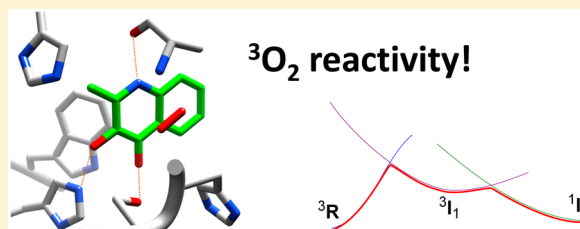
[†]Manchester Institute of Biotechnology and Faculty of Life Sciences, The University of Manchester, 131 Princess Street, Manchester M1 7DN, United Kingdom

[§]Randall Division of Cell and Molecular Biophysics, King's College London, London SE1 1UL, United Kingdom

[‡]Manchester Institute of Biotechnology and School of Chemical Engineering and Analytical Science, The University of Manchester, 131 Princess Street, Manchester M1 7DN, United Kingdom

S Supporting Information

ABSTRACT: Dioxygenases catalyze a diverse range of biological reactions by incorporating molecular oxygen into organic substrates. Typically, they use transition metals or organic cofactors for catalysis. Bacterial 1-*H*-3-hydroxy-4-oxoquinoline-2,4-dioxygenase (HOD) catalyzes the spin-forbidden transfer of dioxygen to its *N*-heteroaromatic substrate in the absence of any cofactor. We combined kinetics, spectroscopic and computational approaches to establish a novel reaction mechanism. The present work gives insight into the rate limiting steps in the reaction mechanism, the effect of first-coordination sphere amino acids as well as electron-donating/electron-withdrawing substituents on the substrate. We highlight the role of active site residues Ser₁₀₁/Trp₁₆₀/His₂₅₁ and their involvement in the reaction mechanism. The work shows, for the first time, that the reaction is initiated by triplet dioxygen and its binding to deprotonated substrate and only thereafter a spin state crossing to the singlet spin state occurs. As revealed by steady- and transient-state kinetics the oxygen-dependent steps are rate-limiting, whereas Trp₁₆₀ and His₂₅₁ are essential residues for catalysis and contribute to substrate positioning and activation, respectively. Computational modeling further confirms the experimental observations and rationalizes the electron transfer pathways, and the effect of substrate and substrate binding pocket residues. Finally, we make a direct comparison with iron-based dioxygenases and explain the mechanistic and electronic differences with cofactor-free dioxygenases. Our multidisciplinary study confirms that the oxygenation reaction can take place in absence of any cofactor by a unique mechanism in which the specially designed fit-for-purpose active-site architecture modulates substrate reactivity toward oxygen.



INTRODUCTION

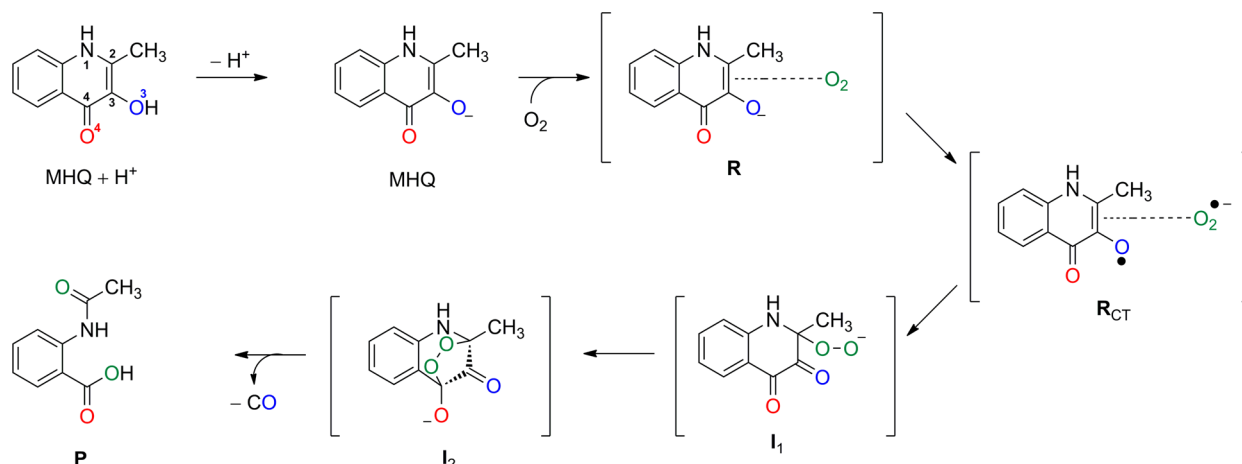
Dioxygenases are mechanistically intriguing enzymes since they are able to perform a spin-forbidden reaction in which the triplet spin ground-state of molecular oxygen reacts with either a cofactor or an organic molecule. These enzymes catalyze the incorporation of molecular oxygen into their organic substrates as a means to initiate their metabolism. Dioxygenases perform key functions for human health and participate in central biochemical functions such as DNA base repair and hypoxia responses.¹ Furthermore, they have been used in the development of new antitumor therapies.² In plants, dioxygenases are essential in signaling mechanisms as well as in secondary metabolism.³ Bacterial dioxygenases, such as naphthalene dioxygenase, are of great interest for their biotechnological applications in contaminated soils, where they are involved in the biodegradation of harmful compounds.⁴ Interestingly, these enzymes show different cofactor requirements, ranging from transition metals (typically iron with either a heme and nonheme ligand environment) to flavins; moreover they show diverse structural frameworks to drive oxygenation chemistry.

Ring-cleaving dioxygenases play critical roles in the aerobic biodegradation of aromatic compounds.⁵ A large subgroup of the ring-cleaving dioxygenases is the catechol dioxygenases that contain nonheme iron as cofactor. On the basis of the cleavage mode and redox state of the cofactor, these are classified in two major groups: (i) the extradiol dioxygenases, which employ Fe²⁺ and cleave adjacent to the vicinal hydroxyl groups of catechols (*meta*), and (ii) the intradiol dioxygenases, which use an Fe³⁺ cofactor and cleave in between the hydroxyl functions (*ortho*) of the substrate. The catalytic mechanism of both groups has been studied in detail by a combination of kinetic,⁶ spectroscopic,⁷ crystallographic,⁸ and computational studies.⁹ Although intra- and extradiol dioxygenases differ in their O₂ activation mechanisms, both converge at an alkylperoxo intermediate. However, since the substrate binding to the iron differs in both groups, the cleavage specificity is altered through the coordination mode.^{8b}

Received: April 14, 2015

Published: May 19, 2015

Scheme 1. Proposed Catalytic Cycle of the Cofactor-Free Dioxygenase HOD



Interestingly, one specific class of ring-cleaving dioxygenases is able to catalyze the breakdown of catecholate-related compounds via oxygen incorporation without the requirement of any kind of cofactor.¹⁰ One example of a cofactor-free oxygenase, is 1-*H*-3-hydroxy-4-oxoquinoline 2,4-dioxygenase (HOD) from *Arthrobacter nitroguajacolicus* R61a, which catalyzes the oxygenolytic breakdown of its natural *N*-heteroaromatic substrate (2-methyl-3-hydroxy-4(1*H*)-quinolone, MHQ) with concomitant release of carbon monoxide. Although details of the catalytic cycle of HOD remain uncertain, the hypothesized cycle based on experimental studies is depicted in Scheme 1.¹¹ The catalytic cycle starts with MHQ binding and its deprotonation at oxygen atom O³. Subsequently, dioxygen binds into the active site (structure R), which is believed to trigger an electron transfer to form the charge-transfer complex R_{CT}. The superoxo group attacks the substrate to form the substrate-peroxo complex (I₁) followed by a ring-closure step to form a bicyclic ring structure (I₂). The latter releases CO and forms the *N*-acetyl-anthranilate product (P).

HOD, together with *Pseudomonas putida* 33/1 1-*H*-3-hydroxy-4-oxoquinoline 2,4-dioxygenase (QDO), constitute a separate dioxygenase family. Structurally, they are not related to any known cofactor-dependent dioxygenase.¹⁰ Instead, they belong to the α/β -hydrolase fold similar to hydrolases,^{11b} and for this reason, HOD and QDO represent fascinating examples of divergent evolution of the α/β -hydrolase architecture from ester hydrolysis to oxygenation reactions.^{10,11b}

The HOD reaction mechanism has been subject to a number of biochemical studies during the past decade.^{11b,c,12} Site-directed mutagenesis and kinetic studies have shown that HOD employs a general base mechanism in which an active site His₂₅₁/Asp₁₂₆ dyad plays an essential role by deprotonation of the hydroxyl group (O³) of the substrate (step 1 in Scheme 1). By contrast, classical α/β -hydrolases react via a nucleophilic reaction mechanism. Figure 1 displays the active site structure of substrate-bound HOD (PDB code 2WJ4), where we inserted the oxygen molecule at the chloride position in the 2WM2 PDB file.^{11b} The substrate is located in a polar active site with several histidine, tryptophan and aspartic acid residues, and consequently is tightly bound through hydrogen bonding interactions including those with the aforementioned His₂₅₁-Asp₁₂₆ dyad. The proton transfer step in the catalytic cycle initiated by this dyad is not rate limiting for the overall reaction,

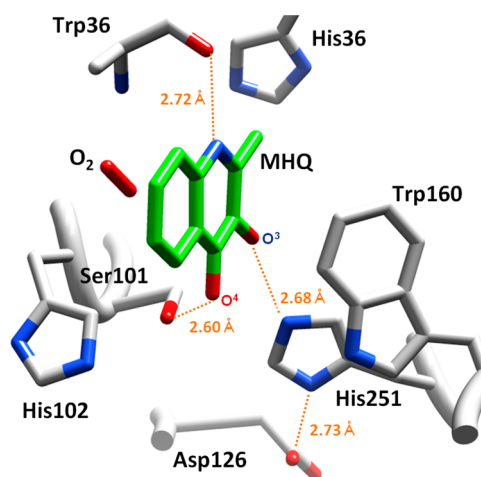


Figure 1. Substrate (MHQ) and dioxygen bound HOD. Active-site residues surrounding the substrates shown in stick representation. The structure is based on the coordinates of the anaerobic HOD·MHQ complex (2WJ4 PDB). The oxygen molecule was inserted at the position of the bound chloride ion as seen in the 2WM2 PDB file.

but is essential for oxygen activation.^{11b,12a,c} Very little is known about the catalytic mechanism after dioxygen binding and how it differs from iron-containing dioxygenases. However, recently, a spin-trap experiment^{11c} found evidence of a short-lived superoxide radical that was tentatively assigned to structure R_{CT} in Scheme 1.

To gain insight into the chemical details of the catalytic mechanism of substrate oxygenation by cofactor-free dioxygenases, we performed a combined experimental and computational study on the O₂ dependent reaction steps of the catalytic mechanism. We particularly focus on the roles played by the conserved active site residues His₂₅₁ and Ser₁₀₁, and the cap domain residue Trp₁₆₀ (Figure 1). The results highlight the important contributions of His₂₅₁ in the catalytic mechanism, namely, as catalytic base for substrate activation, and subsequently as the key residue during the O₂ reaction. We have identified important roles of additional active-site residues (Ser₁₀₁, His₁₀₂ and Trp₁₆₀) that stabilize substrate positioning in the active site through hydrogen bonding interactions, but also enable an effective oxygenolytic substrate cleavage via stabilization of the reaction intermediates through long-range electrostatic interactions. The computational modeling studies

identify details of the reaction mechanism and the critical roles of amino acid residues in the substrate binding pocket. Moreover, they further explain how cofactor-free dioxigenases are able to catalyze an energetically difficult reaction, which is otherwise not known to happen in nature without the assistance of a cofactor.

MATERIALS AND METHODS

Materials. All chemicals were obtained from Sigma-Aldrich unless otherwise stated.

DNA Techniques. The 1-*H*-3-hydroxy-4-oxoquinaldine 2,4 dioxigenase (HOD) cDNA was previously cloned into the pQE30 (Qiagen) vector,^{12c} carrying the C69S mutation to prevent oxidative protein dimerization^{12a} without any effect on HOD activity.^{12b} The corresponding pQE30-wtHOD construct was used to transform *Escherichia coli* M15 [pREP4] strain (Qiagen).

Site-directed mutagenesis was performed following the QuikChange Site-Directed Mutagenesis Kit (Stratagene) protocol, using pQE30-wtHOD as template, and the following primers (direct sequences) with mutations (underlined) at the corresponding triplets (brackets) were used as primers: S101A, 5'-CTTCCGGTATTCAT[GCG]-CACGGCGGCTGGGTTC-3'; W160A, 5'-GCCTGTTCGACGT-[GCG]GCTTGACGGGCATGACG-3'; W160F, 5'-CGGCC-TGTTTCGACGTC[GCG]CTTGACGGGCATGACG-3'; H251A, 5'-GGGCGGGCCGACC[GCC]TTCCCGCCATCGACG-3'. Mutations were confirmed by sequence analysis.

Expression and Purification of HOD Samples. HOD expression and purification was carried out as described previously.^{12c} Protein concentrations were determined spectrophotometrically using an extinction coefficient at 280 nm deduced from the amino-acid sequence: 64 525 M⁻¹ cm⁻¹ for wt HOD, S101A and H251A; 59 025 M⁻¹ cm⁻¹ for W160F/A.

Substrates Analyses. The natural substrate, 3-hydroxy-2-methyl-4(1*H*)-quinolone (MHQ) was synthesized by Sigma at 99.6% purity. The 3-hydroxy-2-butyl-4(1*H*)-quinolone (BHQ) substrate was synthesized by AF ChemPharm (Sheffield, UK) at 97% purity. For determining the molecular extinctions coefficients at pH 8.5 (MHQ $\epsilon_{334} = 9800 \text{ M}^{-1} \text{ cm}^{-1}$, BHQ $\epsilon_{336} = 9700 \text{ M}^{-1} \text{ cm}^{-1}$) the substrates were first dissolved in DMSO (200 mM, MHQ and 10 mM, BHQ) and later diluted in 0.1 M MTE. MTE is a buffer solution containing 2-(*N*-morpholino)-ethanesulfonic acid, Tris and ethanolamine. The BHQ solubility in MTE is restricted to 100 μM , while MHQ solubility limit is 1 mM. MHQ concentration at high absorbance was determined by $\epsilon_{357} = 3300 \text{ M}^{-1} \text{ cm}^{-1}$.

Steady-State Studies. Initial rates of MHQ/BHQ substrate oxygenation by HOD were measured by following the absorbance decrease at the corresponding wavelengths (using the above ϵ values). To determine the kinetic parameters for the aromatic substrates (MHQ/BHQ) the reactions were carried out under atmospheric oxygen concentration at varying substrate concentrations (MHQ, 5–400 μM and BHQ, 5–100 μM) in 0.1 M MTE buffer containing 5 mM NaCl and 2 mM EDTA at 20 °C. Reactions were initiated by adding a small amount (5–10 μL) of concentrated HOD samples to reach the desired concentrations: 15 nM (wt HOD), 18 nM (S101A), 40 nM (W160F), 360 nM (W160A) 8 μM (H251A) and 15 μM (H102A/H251A). Steady-state kinetic constants were obtained by fitting the initial rates at different substrate concentrations to the Michaelis–Menten equation.

To gain further information about HOD catalysis, the initial rates were also determined in the presence of varying concentrations of oxygen (35–1300 μM) at saturated MHQ/BHQ concentration in 0.1 M MTE buffer at 20 °C. Oxygen concentrations were obtained by mixing the desired amount of anaerobic buffer and oxygen saturated buffer (prepared by bubbling buffer with pure oxygen) in a screw-cap cuvette. This procedure was performed inside an anaerobic glovebox. The kinetic parameters were obtained by fitting the initial rates to eq 1,

$$v_{\text{obs}} = k_{\text{cat}}/K_{\text{mO}_2}[\text{O}_2] \quad (1)$$

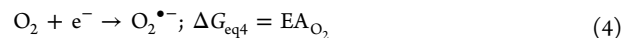
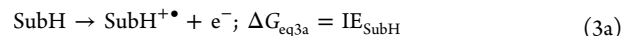
where v_{obs} is the observed turnover rate constant at certain oxygen concentration, k_{cat} is the catalytic constant and K_{mO_2} is Michaelis constant for O₂.

Transient-State Studies. Single-turnover experiments were carried out under anoxic conditions using a TgK Scientific stopped-flow spectrometer maintained in an anaerobic glovebox at oxygen concentrations <2 ppm (Belle Technology). Reactants were prepared inside the glovebox and the enzyme was made anoxic by passing it through a PD-5 column. To achieve a single-turnover reaction, enzyme–substrate (ES) complexes were prepared using a small (20 μM substrate, 30 μM HOD) and large (15 μM substrate, 240 μM HOD) enzyme excess. Oxygen concentrations were obtained by mixing the desired amount of anaerobic buffer and oxygen saturated buffer (prepared as above) in the syringe. The reaction was measured by following the absorbance decrease at 340 nm upon mixing the ES complex and oxygen in 0.1 M MTE, 5 mM NaCl and 2 mM EDTA at 20 °C. The oxygenation constant was obtained from eq 2, where, k_{obs} is the apparent observed rate constant associated with substrate oxygenation at any given concentration of oxygen, and k_{ox} is the second-order rate constant for oxygenation.

$$k_{\text{obs}} = k_{\text{ox}}[\text{O}_2] \quad (2)$$

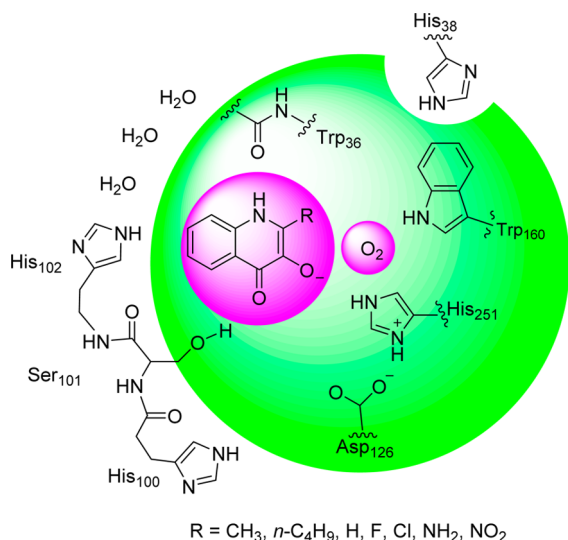
Computational Studies. The calculations reported here were done using density functional theory (DFT) methods as benchmarked and calibrated previously.¹³ All calculations use the *Gaussian-09* program package,¹⁴ with the unrestricted hybrid DFT method UB3LYP in combination with 6-31G and 6-311++G** basis sets, designated as BS1 and BS2, respectively.¹⁵ Full geometry optimizations (without constraints for the oxygen and the aromatic substrate) were performed followed by a frequency calculation at UB3LYP/BS1. All local minima had real frequencies only, and the transition states had one imaginary frequency for the correct mode. Energies reported in this work were obtained with basis set BS2 and contain zero-point corrections. Gibbs free energies were calculated at 1 atm pressure and 298 K temperature, and contain entropic, zero-point and thermal corrections to the energy at basis set BS2. In addition, solvent corrections to the energies were included as obtained from a single point calculation using the polarized continuum model with dielectric constant of $\epsilon = 5.70$ or $\epsilon = 78$. Geometry optimizations of several structures using a dielectric constant of $\epsilon = 78$ gave little changes with respect to the gas-phase optimized structures and energies to within 1 kcal mol⁻¹.

The oxygenation reaction was studied using models of various molecular sizes (Scheme 2). The smallest chemical system (Model A; shown with the purple circles in Scheme 2) only contained substrates with different substituents on the R-position with R = methyl, *n*-butyl, H, F, Cl, NH₂ and NO₂. This model was used in the studies of the substituent effect on the electron transfer step in the reaction mechanism. Hence, we calculated the ionization energy (IE) for the protonated (SubH) and deprotonated (Sub⁻) forms of these substrates, by taking the energy difference between the ionized and nonionized structures. In addition, we calculated the electron affinity (EA) of molecular oxygen as the difference in energy between ²O₂⁻ and ³O₂. We calculated the IE and EA values from the reaction energies of eqs 3a, 3b, and 4:



On the basis of the coordinates of the anaerobic HOD-MHQ and the HOD-chloride complex (PDB entries 2WJ4 and 2WM2, respectively) we created active site models of different size: Models B and C. The smallest model (B) includes the organic substrate, O₂, the side chains of His₂₅₁, Asp₁₂₆, Ser₁₀₁, and Trp₁₆₀ as well as the peptide backbone of Trp₃₆ (total number of atoms: 86). The largest system (model C) studied here is constituted of model B supplemented with the imidazole groups of His₃₈, His₁₀₀, and His₁₀₂,

Scheme 2. Structures of Model A (Purple Circle), Model B (Green Circle) and Model C (All Residues Shown) Used in Our DFT Calculations (See Main Text)^a



^aWiggly lines identify bonds that were cut from the crystal structure. Several of the peptide backbone atoms were kept fixed in the crystal structure coordinates.

as well as three crystal water molecules (total number of atoms: 141). Model C was also modified to get the corresponding variants: W160A (whereby the Trp₁₆₀ group was removed), W160F (Trp₁₆₀ replaced by a toluene group) and S101A (Ser₁₀₁ replaced by methyl group). Structure B was investigated with different protonation states of His₂₅₁, whereby in B₁ His₂₅₁ is doubly protonated and Asp₁₂₆ is deprotonated, in model B₂ His₂₅₁ is singly protonated and lacks the Asp₁₂₆ residue and model B₃ has a doubly protonated His₂₅₁ and no Asp₁₂₆ residue.

Transition state searches were started by initially running extensive geometry scans on the singlet and triplet spin state surfaces between various local minima, whereby one degree of freedom for the reaction coordinate (i.e., the MHQ C²–O₁ distance) was fixed and all other degrees of freedom were fully optimized. The maxima of these scans were then used as starting points for the full transition state searches. Previous studies showed that within transition state theory these free energies of activation can be converted into rate constants that were found to reproduce experimentally determined rate constants of oxygen atom transfer reactions to within 3 kcal mol⁻¹.¹⁶

RESULTS

In this work we applied kinetics, spectroscopic, and computational methods to elucidate the mechanism of dioxygenation by HOD, particularly on the oxygen-dependent steps. The research is focused on the roles of the active-site residues His₂₅₁, Ser₁₀₁ and Trp₁₆₀ by generating site-directed mutants followed by steady- and transient-state studies. Details of the reaction mechanism were established from density functional theory modeling to determine the rate-determining step in the reaction and the quantum mechanical features that affect the height of the barrier, and consequently the rate constant.

Steady-State Studies. First we determined the reaction rate using two different substrates, MHQ and BHQ, at fixed (atmospheric) oxygen concentration. The maximum reaction rate was achieved at high substrate concentrations (Supporting Information, Figure S1) and allowed us to determine the rate constants. Apparent kinetic constants (k_{cat} and k_{cat}/K_m) were determined for active site single variants S101A, W160F, W160A, and H251A and the double variant H102A/H251A for MHQ and BHQ substrates, which enables us to establish the effect of the substituent on catalysis.

As shown in Table 1, MHQ binding is affected by the S101A substitution, which leads to a 48 fold lower k_{cat}/K_m value although both k_{cat} values are similar. The Trp₁₆₀ replacement by phenylalanine or alanine has a direct impact on overall catalysis, as reflected on their reduced k_{cat} values (4 and 65 fold lower than wt, respectively) and k_{cat}/K_m (77 and 5200 fold lower than wt, respectively). The most dramatic change is observed for the H251A and H102A/H251A variants showing a k_{cat}/K_m reduced by 7×10^4 and 4×10^5 fold, respectively. These kinetic parameters and reaction rates are in good agreement with those reported previously.^{11b}

In order to find out how ring-substitution affects the kinetics of substrate activation, we attempted to synthesize additional substrates where the MHQ methyl group was replaced by *n*-butyl (BHQ). For wt HOD, the substitution of MHQ for BHQ does not affect the reaction rate (similar k_{cat} values for MHQ and BHQ). Each variant, however, shows a different behavior. The largest k_{cat}/K_m decrease upon replacing the substrate with BHQ is observed for S101A (16-fold) followed by the W160F (7 fold) and W160A (2 fold).

In addition, we studied the effect of oxygen concentration on HOD catalysis, using the above substrates at saturating concentration. The substrate concentration was different for

Table 1. Apparent Steady-State Kinetic Constants for wt HOD and Its Variants^{a,b}

		k_{cat} (s ⁻¹)	K_m (μM)	k_{cat}/K_m (s ⁻¹ ·mM ⁻¹)
MHQ	WT	26 ± 1	2.1 ± 0.1	12500 ± 600
	S101A	34 ± 1	127 ± 8	265 ± 19
	W160F	7 ± 0.1	41 ± 2	162 ± 10
	W160A	0.40 ± 0.01	170 ± 17	2.4 ± 0.3
	H251A	5.5 ± 0.1 × 10 ⁻³	32 ± 2	0.17 ± 0.01
	H251A/H102A	2.2 ± 0.2 × 10 ⁻³	64 ± 15	0.034 ± 0.009
BHQ	WT	33 ± 1	20 ± 2	1680 ± 190
	S101A	1.7 ± 0.1	101 ± 5	17 ± 1
	W160F	1.3 ± 0.1	57 ± 2	23 ± 2
	W160A	0.8 ± 0.1 × 10 ⁻²	75 ± 10	1.0 ± 0.1
	H251A	1.1 ± 0.1 × 10 ⁻³	57 ± 7	0.20 ± 0.01

^aApparent kinetic constants were determined under atmospheric oxygen in 0.1 M MTE buffer at pH 8.5 supplemented with 2 mM EDTA and 5 mM NaCl at 20 °C. ^bValues reported are the calculated mean ± errors. The errors considered were taken larger than the standard deviation between four replicates and the numerical errors after fitting.

each sample, depending on the K_m value reported above, and the oxygen concentration was varied in the sealed cuvette. In this case, we were not able to observe any reaction rate saturation at high oxygen concentrations (Supporting Information, Figure S2) even when we employed the maximum oxygen dissolved concentration that could be experimentally achieved at 20 °C (1.3 mM), implying that bimolecular association of oxygen to HOD contributes to reaction rate limitation. For that reason, we could only determine the $k_{\text{cat}}/K_{\text{mO}_2}$ constants shown in Table 2. These values not only confirm the effect of the

Table 2. Steady- and Transient-State Oxygen Constants for wt HOD and Its Variants^{a,b}

		$k_{\text{cat}}/K_{\text{mO}_2}$ (mM ⁻¹ ·s ⁻¹) ^c	k_{ox} (mM ⁻¹ ·s ⁻¹) ^d
MHQ	WT	51 ± 2	102 ± 5
	S101A	52 ± 3	57 ± 3
	W160F	13 ± 1	18 ± 1
	W160A	2.0 ± 0.1	1.0 ± 0.1
	H251A	1.7 ± 0.1 × 10 ⁻²	2.1 ± 0.1 × 10 ⁻²
	H251A/H102A	3.1 ± 0.2 × 10 ⁻³	7.3 ± 0.3 × 10 ⁻³
BHQ	WT	50 ± 4	116 ± 6
	S101A	2.0 ± 0.2	3.8 ± 0.2
	W160F	2.0 ± 0.1	4.2 ± 0.3
	W160A	0.13 ± 0.02	0.38 ± 0.03
	H251A	1.8 ± 0.1 × 10 ⁻³	2.2 ± 0.1 × 10 ⁻³

^aConstants were obtained in 0.1 M MTE buffer at pH 8.5 supplemented with 2 mM EDTA and 5 mM NaCl at 20 °C. ^bValues reported are the calculated mean ± error. The errors for transient-state constants were taken larger than the standard deviation between six replicates and the numerical errors after fitting. ^cSteady-state constants were determined at saturated MHQ or BHQ concentration and varying O₂ concentration in the cuvette. ^dTransient-state constants were determined by reacting the ES complexes at different O₂ concentration using an stopped-flow equipment.

mutation observed, but also reflect the above effect of the aromatic substrate (MHQ vs BHQ) on the reaction rate. In all cases, the apparent k_{cat}/K_m values (Table 1) are larger than the $k_{\text{cat}}/K_{\text{mO}_2}$ values (Table 2, left), which implies that the oxygen-dependent reaction steps are rate-limiting. Furthermore, the difference in the $k_{\text{cat}}/K_{\text{mO}_2}$ values observed for the variants (compared to wt HOD) are quite similar to the changes observed for the apparent k_{cat} under atmospheric oxygen concentration, although the absent K_{mO_2} values compromise detailed comparison between samples.

Transient-State Studies. To gain further insight into the oxygen dependent steps during HOD catalysis, we measured the transient absorbance decrease at $\lambda_{\text{max}} = 340$ nm upon mixing anaerobic samples of enzyme–substrate complex with aerobic buffer in a stopped-flow instrument. Two different experimental designs were employed to trap and characterize short-lived intermediates formed during the reaction and to ensure the maximum amount of enzyme–substrate (ES) complex is formed. In the first approach, the ES mixtures contained only a slightly higher amount of enzyme (30 μM) than substrate (20 μM) to explore the contribution of ES complex formation during catalysis. Using this strategy, no distinctive new species could be detected during the oxygenation reaction, which implies that either these species have a spectroscopic signature parallel to the substrate or their lifetime is too short to be detected.

In a second set of experiments, the reaction mixtures were prepared using a large excess of enzyme (240 μM) compared to the substrate (15 μM). A single-exponential decay was observed for all samples tested, and, hence, no distinctive reaction intermediates were observed. However, in these experiments the reaction rates were substantially higher as compared to those observed above (Supporting Information Table S1).

The observed oxygenation rates (k_{obs}) are linearly dependent on the oxygen concentration (Figure 2) for both MHQ and

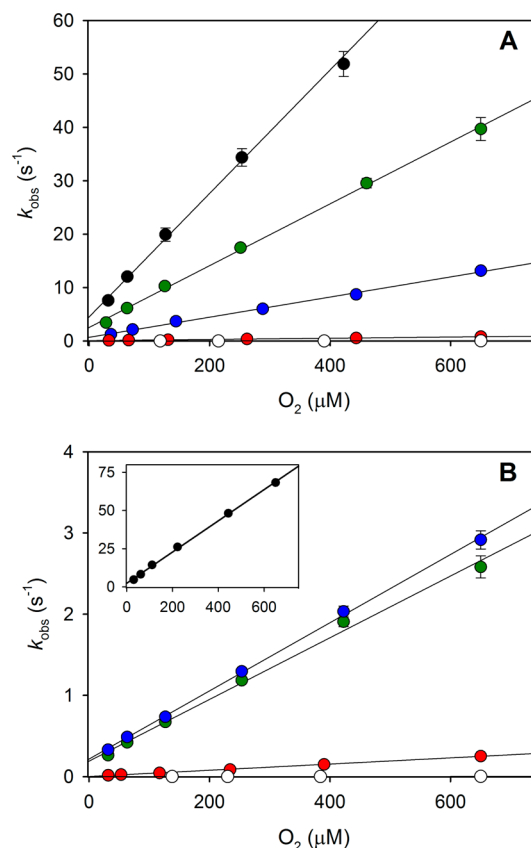


Figure 2. Oxygenation rate dependence on oxygen concentration for wt HOD and its variants. The observed oxygenation rates (k_{obs}) were obtained by reacting the anaerobic enzyme-MHQ (A) and enzyme-BHQ (B) complexes with buffer at different oxygen concentrations using a stopped-flow instrument: wt HOD (black), S101A (green), W160F (blue), W160A (red) and H251A (white). All reactions were measured in 0.1 M MTE buffer pH 8.5, 5 mM NaCl and 2 mM EDTA at 20 °C. The errors considered in the measured rates were taken as the standard deviation of six replicates. Values of k_{ox} (Table 2) were calculated from the gradients of these plots.

BHQ substrates, for this reason only a second-order rate constant (k_{ox}) could be determined (Table 2). The oxygen constants $k_{\text{cat}}/K_{\text{mO}_2}$ (steady-state) and k_{ox} (transient-state), shown in Table 2, are of the same order of magnitude. Consequently, the oxygen-dependent steps are rate-limiting for overall catalysis.

Theoretical Calculations. Density functional theory (DFT) methods were employed to gain additional information about the reaction mechanism and identify the rate-limiting step in the overall catalysis. Furthermore, the calculations establish the role of active site residues in the reaction mechanism and their function to position and stabilize the substrate. The oxygen transfer reaction was studied for wt

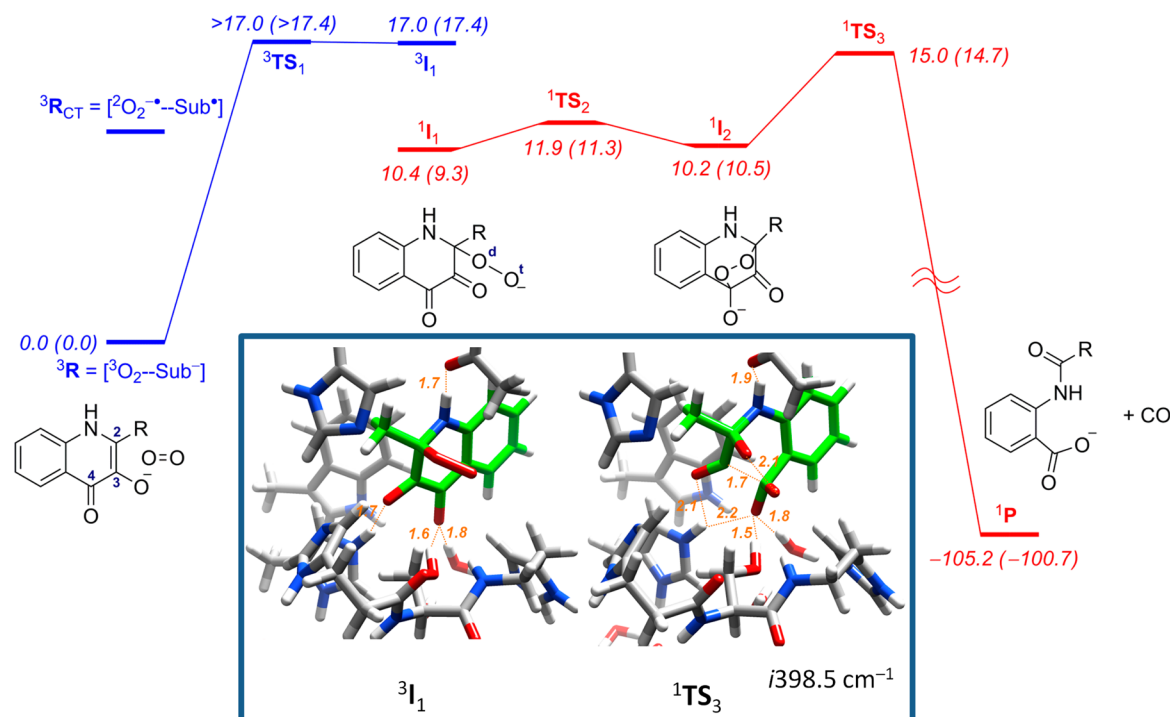


Figure 3. Reaction energy profile and DFT optimized structures of key intermediates and transition states for wt HOD. The reaction energy profile gives Gibbs free energies (gas-phase) and solvent corrected values (in parentheses). DFT optimized geometries of 3I_1 and 1TS_3 are given in the inset and include distances in angstroms and the imaginary frequency in the transition state in wavenumbers. Values shown were determined using UB3LYP/6-311++G** on model C.

HOD as well as the H251A, S101A, W160F and W160A mutants. Additionally, we studied the effect of the nature of the substrate on chemical catalysis through the use of ring-substituted HOD models (HOD^R), whereby the methyl group at position C² was replaced with another substituent R = *n*-Bu, F, and NO₂.

General Catalytic Reaction Mechanism. Our work was initially focused on the catalytic reaction mechanism for MHQ breakdown into *N*-acetyl-anthranilate and carbon monoxide. Upon substrate binding the His₂₅₁-Asp₁₂₆ dyad abstracts the hydroxyl proton from O³, for which we previously calculated a reaction energy $\Delta G = -3.9\text{ kcal mol}^{-1}$.^{12c} It has been suggested that binding of O₂ into the substrate binding pocket leads to an electron transfer from substrate to O₂ and the formation of a superoxo radical anion, as shown in eq 5. We calculated an electron affinity (EA) of 3O_2 of 0.60 eV in the gas phase, which is within 4 kcal mol⁻¹ from the value reported in the literature.¹⁷ With solvent corrections included an electron transfer free energy $\Delta G_{eq5} = 11.2\text{ kcal mol}^{-1}$ ($\epsilon = 5.7$), whereas a $\Delta G_{eq5} = 8.0\text{ kcal mol}^{-1}$ is found when the dielectric constant of water is used. This implies that the electron transfer is an endothermic process and unlikely to happen spontaneously in the protein or in solvent.



To investigate how the protein and, in particular, the local environment affects the electron transfer in reaction 5, we set up a set of models with increasing size and protein description. Our simplest models take substrate and oxygen in isolation (model A), but in subsequent models the local protein environment is taken into consideration using models B and C (Scheme 2). Thus, in both reactant models B and C the calculations converge to an electronic ground state that is best

described as an $[^3O_2-Sub^-]$ complex with a spin density of approximately 1.6 on the O₂ moiety and the rest on the substrate: $\rho_{O3} = 0.13$, $\rho_{C2} = 0.10$, $\rho_{O4} = 0.05$ and $\rho_{C4} = 0.04$ (see Supporting Information Table S10). Therefore, close approach of O₂ onto the MHQ group leads to a minor redistribution of charges and electronic spins, but retains most of the original electronic description of the reactants. To further confirm that the charge-transfer state (right-hand-side of eq 5) is an excited state, we swapped molecular orbitals and attempted to converge the wave function of the reactant complex to the charge-transfer complex, R_{CT} . However, during the SCF convergence the wave function converged back to the reactant configuration with a triplet spin O₂ complexed to a closed-shell singlet substrate anion. Therefore, even with the protein environment included, the substrate-dioxygen complex is unable to form spontaneously by electron transfer, and, consequently any reactivity of O₂ will come from dioxygen and not from the stabilization of a radical pair.

Subsequently, we calculated the mechanism of dioxygen transfer to MHQ as described in Scheme 1 using models B and C with DFT methods. The obtained results starting from the triplet spin reactant complex 3R are schematically depicted in Figure 3. The reaction starts with attack of dioxygen on carbon C² of MHQ via a barrier 3TS_1 , to form the superoxide complex 3I_1 . The latter is a very shallow minimum below 3TS_1 . However, detailed geometry scans indicated 3TS_1 to be close in energy to 3I_1 (see Supporting Information Figure S4). Electronically, 3I_1 can be described as a biradical with radical character on the terminal oxygen atom of the peroxy group ($\rho = 0.69$), while there is spin of 0.32 on the distal oxygen atom and the rest on the substrate: $\rho_{O3} = 0.30$, $\rho_{C3} = 0.14$, $\rho_{O4} = 0.21$ and $\rho_{C4} = 0.24$. Upon formation of 3I_1 from 3R , therefore, a minor increase of radical character on O³ is observed that reduces its charge and

weakens the hydrogen bond between O³ and the proton of His₂₅₁ (Nε2), which elongates from 1.64 Å in ³R to 1.72 Å in ³TS₁. The other geometrical change from ³R to ³I₁ relates to elongation of the bonds associated with carbon C², as it is rehybridized from sp² to sp³. It may very well be that the experimentally trapped radical^{11c} is the ³I₁ state described here.

The formation of ³I₁ encounters the highest barrier along the reaction mechanism ($\Delta G^\ddagger = 17.4$ kcal mol⁻¹ in a solvent model), and hence is the rate limiting step for wt HOD catalysis. As shown in Figure 3 the substrate is located in a tight substrate binding pocket and is stabilized via several hydrogen bonding interactions with active-site residues, such as His₂₅₁, Ser₁₀₁ and His₁₀₂ as well as several water molecules. The ring-closure step on the triplet spin state surface to form ³I₂ via ³TS₂ is energetically high in energy (>50 kcal mol⁻¹, see Supporting Information Figure S4), and therefore, the mechanism will not proceed further on the triplet spin state surface. However, a lower energy singlet spin pathway exists and a spin crossing from ³I₁ to ¹I₁ continues the mechanism on the singlet spin state surface. Although we made attempts to calculate the minimum energy crossing point from ³I₁ to ¹I₁, we were not able to locate it precisely, but predict it to be around +10 kcal mol⁻¹ above ³R (Figure S4). We, therefore, expect a fast equilibration and conversion from triplet to singlet in or around ³I₁. Structure ¹I₁ has a strongly elongated O–O distance of 1.56 Å, but only minor geometric changes in the substrate moiety are found with respect to ³I₁.

In the next reaction step, the terminal oxygen atom (O_t) of the peroxy group attacks the keto carbon atom C⁴ with a small barrier (¹TS₂) of 1.9 kcal mol⁻¹ in solvent to form the bicyclic ring-structure, ¹I₂. The transition state (¹TS₂) has a small imaginary frequency of *i*67.5 cm⁻¹ for the C⁴–O_t bond formation, which implicates that the energetic barrier is broad. At the same time as the C–O bond formation there is also a motion for the C³–O³ group that bends it out of the plane of the substrate group due to changes in hybridization of C³ from sp² to sp³ and will eventually leave as a CO molecule. In ¹I₂ the dioxygen bond has weakened to 1.61 Å, while the C⁴–O⁴ distance has grown to 1.36 Å. In this endoperoxide intermediate the dioxygen bond is also weakened similar to what is seen in nonheme iron dioxygenases¹⁸ and breaks to form products P via transition state ¹TS₃.

The last reaction step, namely release of CO and substrate breakdown to the corresponding product, takes place through a small energetic barrier (5 kcal mol⁻¹) from ¹I₂. The imaginary mode for this transition state (¹TS₃) represents the simultaneous dioxygen bond cleavage (O–O stretch) and C³–C⁴ bond breaking, although the C²–C³ distance stays virtually intact at a similar value as in ¹I₂. As such, the CO release from complex ¹I₂ will be accomplished by a stepwise bond breaking process of the initial C³–C⁴ bond followed by the C²–C³ bond. However, no local minimum was found for this process and indeed a geometry scan showed a gradual decrease in energy for the CO release. Structurally (inset in Figure 3), the O–O bond has broken (distance of 2.08 Å) but also the C³–C⁴ bond is elongated strongly (1.73 Å). Both ³I₁ and ¹TS₃ are placed in a similar orientation relative to most active site residues, except for His₂₅₁ which, in the ¹TS₃ bridges O³ and O⁴ at almost equal distances (2.1 Å).

To further establish the roles of the substrate and active site residues on the reaction mechanism and catalysis, we created computational mutants and substrate-analogues and repeated the calculations for the catalytic cycle.

The Function of His₂₅₁. In previous work, we identified an important role of the His₂₅₁-Asp₁₂₆ dyad in regulation the protonation state of the substrate and thereby initiating the catalytic cycle.¹² To explore the role of His₂₅₁ during the oxygen-dependent reaction steps, we did a further set of calculations on model B, whereby His₂₅₁ was chosen in different protonation states: (i) Model B₁ contains the His₂₅₁-Asp₁₂₆ groups and has the Nδ1 atom of His₂₅₁ protonated (proton shared with Asp₁₂₆); (ii) Model B₂ has the Nδ1 atom of His₂₅₁ deprotonated and excludes Asp₁₂₆; (iii) Model B₃ has the Nδ1 atom of His₂₅₁ protonated and does not contain the Asp₁₂₆ residue. Figure 4 displays the calculated reaction mechanism of oxygen insertion into MHQ substrate by models B₁, B₂ and B₃ as well as the full model C.

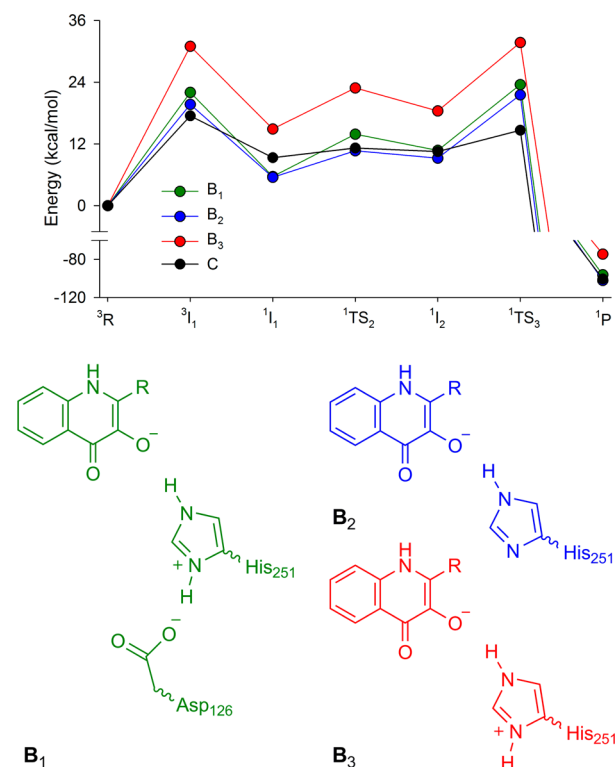


Figure 4. Free energy profiles of oxygen inserting into MHQ as affected by a varying protonation state on His₂₅₁. Values shown were determined using UB3LYP/6-311++G** with solvent corrections included. At the bottom we highlight the structural differences of the catalytic triad for models B₁, B₂ and B₃.

In general, model C, B₁ and B₂ give the same overall reaction mechanism with similar free energy values of local minima and transition states. The only noteworthy changes are a slight increase of ³I₁ (by just over 4 kcal mol⁻¹) and a somewhat larger increase of ¹TS₃, which becomes competitive with the initial barrier. Therefore, second sphere amino acids, such as His₃₈, His₁₀₀ and His₁₀₂ as well as the additional solvent water molecules, have a stabilizing effect on the overall structure.

The major difference, however, is obtained when model B₃ is selected, and the most plausible reason is because this model is charge neutral whereas the other models have an overall charge of -1. These additional Coulombic interactions are expected to give major differences to the energetics. This raises all local minima and transition states dramatically, and, hence, the protonation state of the His₂₅₁ residue is crucial for a correct

description of the enzyme reaction mechanism. During the reaction, the chemical structures of local minima and transition states are similar, which suggests that the energy differences between model B₁, B₂ and B₃ are related with the His₂₅₁ protonation for each system during the reaction. All together these results indicate that His₂₅₁ not only acts as a catalytic base, but, furthermore, it acts as catalytic conjugated acid for effective oxygen insertion into MHQ.

The Function of Trp₁₆₀ and Ser₁₀₁. In order to find out what the function of active site residues Trp₁₆₀ and Ser₁₀₁ is, we created computational mutants of models C for the following variants: W160A (the Trp₁₆₀ description was removed), W160F (indole group representing Trp₁₆₀ was replaced by toluene) and S101A (hydroxyl was replaced by methyl). For each of these variants the full mechanism of MHQ oxygenation and breakdown was studied computationally.

Figure 5 shows the free energy profiles for model C as calculated for wt, W160A, W160F and S101A. Active site

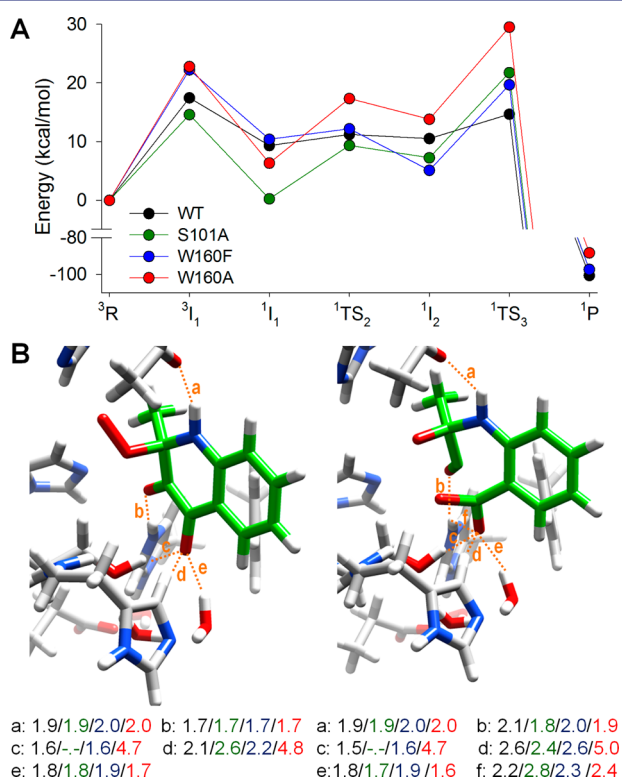


Figure 5. Reaction energy profiles and DFT structures for wt HOD and its variants. (A) Reaction energy profiles for: wt HOD (black), S101A (green), W160F (blue) and W160A (red). (B) ³I₁ (left) and ¹TS₃ (right) optimized geometries (W160F system) including distances between the intermediates (green), active site residues and water (CPK colors). Distances compiled for all systems using same colors as in (A). Optimized geometries and energy values were determined using BS1 and BS2, respectively.

mutants give differences in chemical reaction and particularly regarding the rate-determining step. The energy profiles for the W160F/W160A systems give elevated free energies for ³TS₁ and ¹TS₃ of 4.8/5.4 kcal mol⁻¹ and 5.0/14.8 kcal mol⁻¹, respectively, as compared to wt HOD. In the case of the S101A mutant, the peroxy bound complexes (³I₁ and ¹I₁) are stabilized in energy, while ¹TS₃ is raised by 7.0 kcal mol⁻¹ with respect to wt HOD. Consequently, the S101A system will be more efficient during the C–O bond formation, but much less

effective in substrate breakdown in comparison with wt HOD. Thus, the rate-determining step in the reaction mechanism for wt and W160F is the first barrier (³TS₁) and attack of ³O₂ onto the substrate. By contrast, the active site mutations W160A and S101A considerably destabilize the CO release from ¹I₂ and ¹TS₃ is raised in energy. In particular, the hydrogen bond of Ser₁₀₁ to O⁴ in wt leads to a charge donation toward the substrate (Q_{O4} = -0.68), which drops to Q_{O4} = -0.61 in S101A. At the same time the charge on O³ is more negative in S101A as compared to wt (Q_{O3} = -0.32/-0.38 in wt/S101A) and this makes the release of CO more difficult and hence raises ¹TS₃ in energy.

The comparison of structures ³I₁ and ¹TS₃ (Figure 5B) gives further information on the changes in relative energies along the mechanism. The structure of ³I₁ is similar for wt HOD and W160F systems, whereas geometric changes are encountered for S101A and W160A mutants. In the calculations for the W160A system, due to removal of a bulky tryptophan group, the substrate reorients and the Ser₁₀₁–O⁴ hydrogen bond is lost. In summary, the active site mutations reveal the importance of Ser₁₀₁ and Trp₁₆₀ for positioning and constraining the substrate into a specific orientation. Furthermore, the Ser₁₀₁–O⁴ hydrogen bond donates negative charge to O⁴ and, thereby, pulls CO away from the complex.

In structure ¹TS₃, the substrate positioning is shifted for S101A and W160A systems, where the distances between O⁴ and Ser₁₀₁/His₁₀₂/His₂₅₁ have changed. As above, the Trp₁₆₀ and Ser₁₀₁ residues play an important role in the reaction mechanism by stabilizing the reaction intermediate. Additionally, the His₂₅₁ establishes a new interaction with O⁴, and together with His₁₀₂ enables the intermediate to breakdown into the corresponding products.

The calculated potential energy profiles of wt and mutants compare well with the experimental rate constants shown in Table 1. Thus, in wt the rate-determining step (via ³TS₁) has a free energy of activation of 17.4 kcal mol⁻¹, whereas it is 22.2 kcal mol⁻¹ for W160F. By contrast, for S101A and W160A, the rate-determining step becomes ¹TS₃ with barriers of 21.7 and 29.5 kcal mol⁻¹, respectively. As such, the calculations predict that the rate-determining steps will increase by 4.3, 4.8, and 12.1 kcal mol⁻¹ for S101A, W160F and W160A, respectively. Using transition state theory, the experimental rates from Table 1 implicate increase of the free energy of activation for these mutants by 2.3, 2.6, and 5.1 kcal mol⁻¹, respectively. The calculations, therefore, reproduce the experimental trends well and predict similar rate decreases.

Effect of Substrate on the Reaction Steps. In a final set of calculations, we decided to explore the effects of electron donating/electron withdrawing groups on the *N*-heteroaromatic substrate, whereby the methyl group at C² was replaced by either *n*-butyl, fluoro or nitro groups. The reaction mechanism of substrate dioxygenation was recalculated for model C with these three alternative substrates HOD^X, X = *n*-butyl, F or NO₂. All reactions follow the same mechanism as in the previous sections, but the relative energies of the various structures fluctuate dramatically, Table 3. Part of this is due to electrostatic interactions and partially due to changes in electron donating properties of the substrate.

Table 3 gives relative free energies of key intermediates along the reaction mechanism for the four calculated substrates. As can be seen, the rate-determining step is via ³TS₁ for wt as well as HOD^{NO₂}, whereas the release of CO becomes rate determining for HOD^{*n*Bu} and HOD^F. Note that in all cases

Table 3. Solvent Corrected Gibbs Energy Values for Model C HOD^{Ra}

R	³ TS ₁	¹ I ₁	¹ TS ₃	¹ P
Me	17.4	9.3	14.7	-100.7
<i>n</i> -Bu	26.8	16.6	33.6	-103.1
F	11.1	1.1	18.0	-92.9
NO ₂	26.9	16.0	25.2	-87.0

^aEnergy $\Delta G(\text{solv})$ values for model C, HOD^R where R is Me, *n*-Bu, F, NO₂, were calculated using UB3LYP and BS2.

the energy difference between ³TS₁ and ¹I₁ stays virtually the same, so that substrate substitution does not affect the spin state change from triplet to singlet and the spin state ordering, but only affects substrate binding to the active site pocket.

Addition of electron withdrawing groups to the HOD substrate strongly affects the charge of carbon C² in ¹TS₃, whereby $Q_{C^2} = 0.29$ for HOD^{Me}, but values of 0.57, 0.45, and 0.30 are found for HOD^F, HOD^{NO₂} and HOD^{*n*Bu}, respectively. In particular, the latter substrate (BHQ) encounters strongly electrostatic interactions with protein residues in the substrate binding pocket and gives elevated energies and transition state energies along the full reaction mechanism as compared to the natural substrate. This is in agreement with the drop in rate constant reported in Tables 1 and 2.

Finally, Figure 6 displays a Hammett plot for the free energy for ¹TS₃ with respect to the Hammett parameter σ_p .¹⁹ A linear

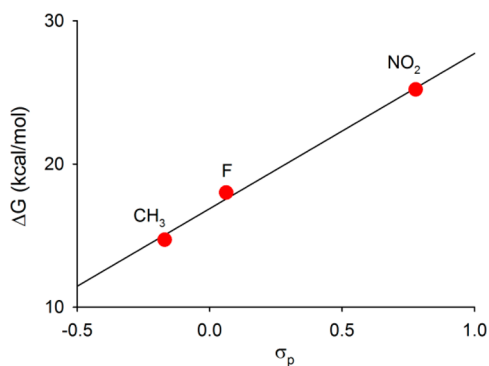


Figure 6. Hammett plot of the free energy for ¹TS₃ as a function of Hammett parameter for different substrates HOD^R, R = CH₃, F and NO₂.

correlation is observed for substitution of the methyl group of MHQ by either F or NO₂. The correlation implies that the barriers ¹TS₃ are affected by the nature of the substituent on the C² position. Moreover, the linear correlation implicates that substitution of methyl by fluoro or nitro incurs no stereochemical interactions with the protein and only affects the reaction through electron-donation. The substrate binding pocket, therefore, can accommodate substrates with the methyl group of MHQ replaced by fluoro or nitro, but a substitution with a much larger group, such as, *n*-butyl distorts the protein substrate interactions considerably.

DISCUSSION

The majority of ring-breakdown oxygenases require an organic or metallic cofactor for their catalytic activity. However, several dioxygenases have been found to perform similar reactions in a cofactor-independent fashion. These class of dioxygenases and monooxygenases are interesting enzymes for biotechnological

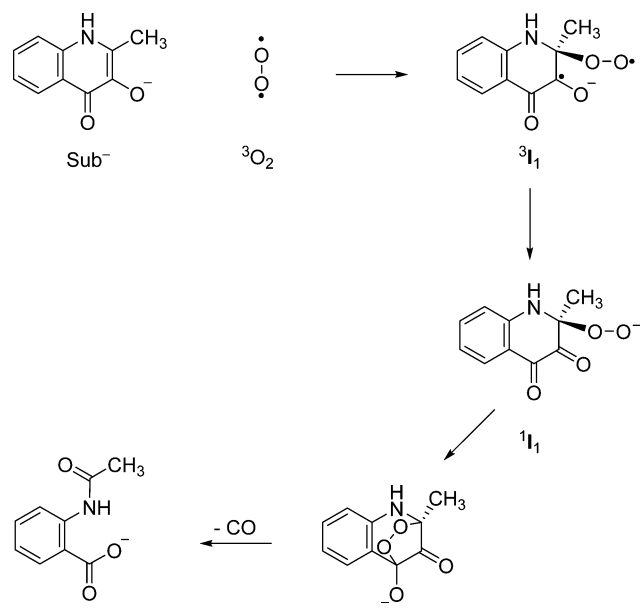
applications, since they do not require cofactors/coenzymes, even if their restricted substrate specificity limits their applicability.²⁰ In particular, their catalytic mechanism is chemically intriguing and in this work, a combined experimental and computational study, is presented on the reaction mechanism of a cofactor independent dioxygenase. In addition, a comparison will be made between cofactor-independent/dependent dioxygenases.

Kinetic Constants. From the comparison of the steady-state kinetic constants k_{cat}/K_m values for the aromatic substrates and O₂, it is observed that the oxygen dependent steps are rate limiting the overall catalysis in agreement with former studies^{12a} and other dioxygenases.²¹ In previous studies using different approaches, whereby both substrates concentrations (MHQ and O₂) were simultaneously varied, a ternary complex mechanism and a K_{mO_2} value $\sim 900 \pm 100 \mu\text{M}$ were determined for wt HOD.^{12a} This K_{mO_2} value is similar to that reported for human²² and bacterial²³ dioxygenases. However, in all cases mentioned, the K_{mO_2} value was close to the maximum concentration of O₂ that could be experimentally achieved, hence these K_{mO_2} values are likely subject to large experimental errors. In any case, the K_m values for the aromatic substrate were 2 orders of magnitude lower than the values for O₂, clearly indicating that the ternary complex formation is limited by the O₂ availability. Furthermore, the O₂ kinetic constants obtained under multiple-turnover (k_{cat}/K_{mO_2}) and single-turnover (k_{ox}) conditions are similar, confirming again that the O₂ dependent steps are rate-limiting in the overall catalysis and in addition suggest that other catalytic steps may have minor effect during the overall turnover, in agreement with previous studies.¹² As discussed above, the observed rate values (k_{obs}) under transient-state conditions are linearly dependent on O₂ concentration. Similar tendencies were observed in flavin-dependent monooxygenases²³ and nonheme iron-dependent dioxygenases.^{6a,8b} Surprisingly, the second-order rate constants calculated for the above enzymes are similar ($\sim 10^5 \text{ M}^{-1} \text{ s}^{-1}$), which highlights the efficient oxygenation chemistry performed by HOD even in the absence of any cofactor.

Using the stopped-flow technique we could successfully monitor a single-turnover reaction by mixing an anaerobically preformed ES complex with O₂. The absorbance decrease observed was assigned to the substrate oxygenolytic cleavage. This decay perfectly fitted to a single-exponential decay, indicating that none of the reaction intermediates were detected, the reason might be their transient lifetime or that their absorbance spectra is not substantially different (as suggested from the measurements using the photodiode array detector). By contrast, the reaction intermediates have been successfully characterized and detected in nonheme iron dioxygenases, where these intermediates have distinguishable kinetic and spectroscopic features,^{6b,24} or were trapped in crystal structures.⁸ Hence, we performed several computational calculations to further investigate the reaction intermediates and rate limiting steps.

Catalytic Mechanism. We suggest a mechanism that starts with an initial deprotonation of the substrate O³ position and binding of ³O₂ at the active site pocket. The mechanism after O₂ binding is summarized in Scheme 3. This work gives no evidence of an initial radical pair formation (long-range electron transfer between ³O₂ and MHQ) but instead the ³O₂ attacks MHQ C² atom to form a C–O bond as a peroxo in a triplet

Scheme 3. Proposed Catalytic Mechanism of HOD on the Basis of Computational, Kinetics and Previous Structural Studies



spin state (3I_1 , peroxy-biradical). Subsequently, an internal electron transfer leads to a closed-shell singlet (1I_1) peroxide intermediate. The terminal oxygen atom attacks carbon C^4 to form an endoperoxide intermediate (1I_2) that releases CO and leads to products. The detailed reasoning for this mechanism is discussed below.

Valence Bond Rationalization of Mechanism. In order to fully understand the details of the initial step in the reaction mechanism, i.e., the steps from $^3R \rightarrow ^3I_1 \rightarrow ^1I_1$, we set up a valence bond (VB) curve crossing diagram (Figure 7). Similar

diagrams were used previously to rationalize the rate constant of hydrogen atom abstraction and double bond epoxidation reactions by metal-oxo complexes, and are particularly useful to understand the electron transfer mechanisms during reaction mechanisms.²⁵ The VB curve crossing diagram starts from our reactant complex (3R), which contains deprotonated MHQ and triplet oxygen. The substrate (Sub) is in a singlet spin state and the π -bond that is being activated in the reaction mechanism is highlighted with the two dots along the bond. The product VB state for this reaction step is the singlet spin peroxy complex 1I_1 (Figure 7, right) and has a wave function $^1\Psi_{Ps}$. In comparison to the reactants structure, one electron from C^2 forms a bond with one of the unpaired electrons of O_2 , and at the same time, the π electron from C^3 forms a π -bond with O^3 . Because of this reorganization one electron has transferred from O^3 to the terminal oxygen atom of the peroxy group. These VB descriptions can now be used to estimate the barrier height for the direct conversion of reactants to 1I_1 through curve crossings. Thus, the product wave function connects to an excited state in the reactant geometry (wave function $^1\Psi_{CT}$) and the reactant wave function connects to an excited state in the product geometry (wave function Ψ_{P^*}). The point where these two curves cross leads to an avoided crossing and a transition state for the reaction. Hence, the crossing of the blue and green lines in Figure 7 leads to a transition state for conversion of 3R into 1I_1 . However, in our diagram there is another, lower-lying VB curve (purple line) that bisects the curves between 3R and 1I_1 and generates a local minimum for 3I_1 and leads to a stepwise process.

The height of the barrier (ΔE^\ddagger) can be estimated from the crossing point of the two curves and was shown to be proportional to a fraction (f) of the excitation energy (G) in the reactant geometry from the ground state to the product state minus a correction for the resonance energy (B) for the change in geometry from reactants to transition state.²⁶ A careful

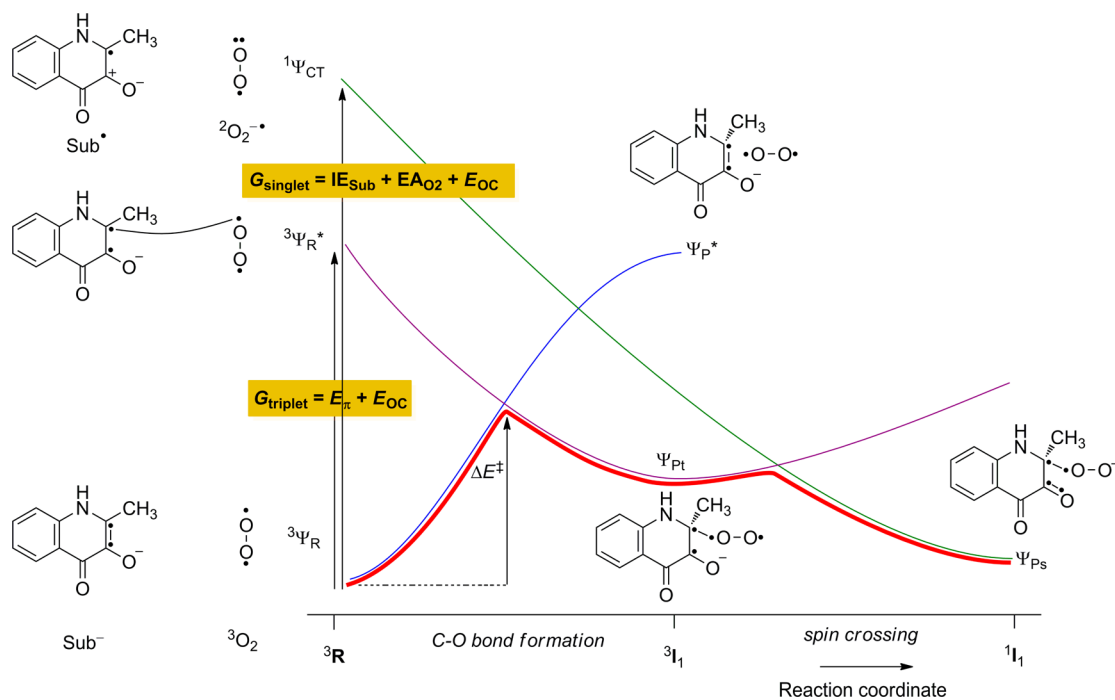


Figure 7. Valence bond curve crossing diagram for the formation of a singlet spin peroxy complex from reactants. Dots represent relevant valence electrons and lines between dots are bonds.

analysis of the VB structures for the reactants (${}^3\Psi_{\text{R}}$) and the excited state products that connect to ${}^3\text{I}_1$, i.e., ${}^3\Psi_{\text{R}}^*$, reveals the intrinsic chemical properties that determine the barrier height. Thus, the transition from ${}^3\Psi_{\text{R}}$ to ${}^3\Psi_{\text{R}}^*$ represents the breaking of the π -bond of the C^2 – C^3 bond (E_{π}) as well as the pairing of the two radicals from C^2 and one of the oxygens of O_2 (E_{OC}), eq 6.

$$G_{\text{triplet}} = E_{\pi} + E_{\text{OC}} \quad (6)$$

The alternative direct pathway from ${}^3\text{R}$ to ${}^1\text{I}_1$ will incur a much larger barrier due to higher energy excitation energy G_{singlet} from ${}^3\Psi_{\text{R}}$ to ${}^1\Psi_{\text{CT}}$. A comparison of the VB structures for the wave functions ${}^3\Psi_{\text{R}}$ and ${}^1\Psi_{\text{CT}}$ gives excitation energy (G_{singlet}) for the ${}^3\text{O}_2$ electron affinity and the substrate ionization potential. In MHQ, G_{singlet} is higher in energy than G_{triplet} and, consequently the reaction will be stepwise with an initial C–O bond formation to form ${}^3\text{I}_1$ followed by an internal electron transfer to form ${}^1\text{I}_1$. Everything together suggests that the spin forbidden reaction between ${}^3\text{O}_2$ and ${}^1\text{Sub}^-$ is bypassed through the approach of both substrates in the active site, which only leads to an electron transfer from ${}^1\text{Sub}^-$ to ${}^3\text{O}_2$ after the peroxy-biradical intermediate is formed. The latter seems to be the actual species formed in this reaction step instead of a caged radical pair (superoxide and substrate radical) as proposed previously.^{11c}

Substituted Substrates. On the basis of Figure 7, it can be anticipated that changing the substituent at C^2 from methyl to an electron-withdrawing or electron-donating group should affect the ionization potential of the substrate and consequently the π -energy E_{π} . Indeed, the calculated ionization energies of C^2 -substituted substrates follow a linear correlation with Hammett σ_{p} -values (Supporting Information, Figure S3). In contrast, the fact that DFT calculations on HOD^{X} , $\text{X} = \text{CH}_3$, $n\text{-C}_4\text{H}_9$, F and NO_2 , found no linear correlation for barrier ${}^3\text{TS}_1$ with the Hammett σ_{p} -value, implicates that both E_{π} and E_{CO} are influenced by the substituent on C^2 . As reported above, addition of an n -butyl substituent (BHQ) had neither effect on the charge nor the electron affinity of the substrate. Instead, we observed strong electrostatic interactions between BHQ and the active site residues which gave elevated energies along the whole reaction profile compared to the natural substrate. The latter computational observations can explain the shift in the rate constants observed here when the BHQ substrate was assayed, in agreement with the literature.^{11c}

Role of His₂₅₁, Ser₁₀₁ and Trp₁₆₀. To gain further insight into the reaction mechanism, we studied the role of several active site residues, including the conserved residues His₂₅₁ and Ser₁₀₁,¹² which correspond to the histidine/nucleophile residues²⁷ of the catalytic triad in the α/β fold superfamily, and the active site residue Trp₁₆₀. The kinetic constants obtained for the H251A variant were 4 orders of magnitude lower than wt HOD, in line with previous experimental observations, which concluded that His₂₅₁ is crucial for catalysis acting as catalytic base.^{11b,15c} As the reaction in H251A is affected at the first catalytic step (substrate deprotonation) we were expecting to shift the rate-limiting reaction step and hence, observe a saturation of the reaction rate at high O_2 concentrations. Instead, the apparent $k_{\text{cat}}/K_{\text{m}}$ value is ten times higher than the corresponding $k_{\text{cat}}/K_{\text{mO}_2}$ value, which strongly suggests that the O_2 -dependent steps are rate limiting the reaction rate in this variant similar to what is observed for wt HOD. Then, why does this initial step have a major impact on

the later reaction with oxygen? To address this question, we compared the ionization potentials of the protonated and deprotonated substrates and found that those values are considerably higher in energy for the protonated substrates than for deprotonated ones. Thus, the ionization potential of neutral MHQ in solvent is calculated to be 5.94 eV, whereas that for the deprotonated structure is only 3.67 eV under the same conditions. Therefore, the deprotonation step in the catalytic cycle is essential for weakening the π -system of the substrate, which then enables subsequent oxygen addition.

In addition, when we compared the reaction energies in the presence of different protonation states of His₂₅₁ (Model B) we observed higher energies and activation barriers for the neutral system (Model B₃) than those for a negatively charged system (Models B₁ and B₂). The effect is the strongest for the first reaction barrier (${}^3\text{TS}_1$) for C–O bond formation, while little changes are observed in the later parts of the mechanism (e.g., for ${}^1\text{TS}_3$). Our results implicate multiple roles for His₂₅₁, namely as catalytic base to drive substrate deprotonation, but also to polarize the C^3 – O^3 bond which activates the substrate C^2 – C^3 π -bond and triggers the electron transfer to O_2 .

When the active site is mainly neutral, as in several flavooxidases, it has been shown that either a double-protonated His, positively charged Lys residue or substrates are essential during the initial electron transfer from reduced flavins to O_2 .²⁸ In these enzymes, a neutral environment around the flavin cofactor helps to control the O_2 electrostatics by creating specific polarization sites around the flavin C^{4a} and N^5 atoms. On the other hand, in HOD, several hydrogen bonding interactions between the aromatic substrate and polar residues (N^1 –Trp₃₆, O^3 –His₂₅₁ and O^4 –Ser₁₀₁) are indeed modulating the substrate electrostatics and hence O_2 reactivity, in which the O^3 –His₂₅₁ bond plays a major contribution.

In this study, we investigated the role of the conserved residue Ser₁₀₁ and the active site residue Trp₁₆₀. The rate constants for the S101A variant were similar to those observed for wt HOD, which suggests that the residue plays a minor role during catalysis. However, the increase in the K_{m} value for MHQ (60 fold) and the reactivity decrease against BHQ (30 fold) suggest that this residue might be involved in the positioning/stabilization of the reaction intermediates. When we compare different model C structures, it is found that when Ser₁₀₁ undergoes hydrogen bonding interactions to O^4 (as in WT and W160F models) the whole reaction profile is low in energy. This hydrogen bond seems to facilitate the endoperoxide breakdown (larger value of ${}^1\text{TS}_3$ in the S101A system) instead of contributing during the initial reaction steps. Noticeably, in the S101A system the negative charge in the intermediates, i.e., in ${}^3\text{I}_1$ and ${}^1\text{I}_2$, is stabilized via interactions of the O^4 atom with an H_2O molecule, which suggests that this new interaction can partially mimic the role of Ser₁₀₁ and thereby explains the similarity of the rate constants of wt HOD and S101A. In the α/β fold hydrolases, the role of the catalytic triad serine residue differs, i.e., in α/β -fold lipases and serine-proteases this residue is performing a nucleophilic attack on the substrate, and has a central role during the catalysis as shown in mutagenesis studies.²⁹ In other cases, as in MhpC and BphD hydrolases, the serine residue either stabilizes the oxyanion intermediate via hydrogen bond or contributes to its protonation.³⁰ Importantly, the structure comparison between HOD (PDB 2WJ4) and MhpC (PDB 1U2E) reveals that the distance between His₂₅₁ ($\text{N}\epsilon$) and Ser₁₀₁ ($\text{O}\gamma$) is similar (3.39 and 3.26 Å, respectively) while this distance in typical serine

proteases is much shorter (2.7 Å).³¹ This structural difference suggests that weakening the interaction between these two conserved residues, the serine is no longer able to act as nucleophile. Hence, this loss of function in the serine is promoting its role hydrogen bonding the reaction intermediates.

Additionally, we generate two different variants (W160F/W160A) to study the Trp₁₆₀ involvement in catalysis. The phenylalanine substitution only partially affects the overall activity while the substitution by a less bulky residue (alanine) decreases the activity dramatically. The corresponding energy profiles for the W160F/W160A models were shifted with respect to wt HOD, and show increased barriers for ³TS₁ and ¹TS₃, and thus affect the O₂ activation mechanism. The crystal structure coordinates locate the Trp₁₆₀ residue in the cap domain and contributes to the shape of the active site pocket.^{11b} This, together with the fact that Trp₁₆₀ does not directly interact with the substrate, suggest that its function might be restricting the position of the substrate favoring its orientation toward catalytically relevant residues (His₂₅₁). As HOD and QDO perform chemically similar reactions, it is interesting to note that another tryptophan residue (Trp₁₅₃) occupies a similar position and orientation in QDO, but little is known of its function. Noteworthy, additional active site residues, such as His₁₀₂ in HOD and His₉₆ in QDO, have been found to contribute to the overall catalysis through mutagenesis studies reported previously.^{11b,12b} Absence of His₁₀₂ (as in Models B) appears to increase the barrier for endoperoxide breakdown, i.e., ¹TS₃, by 8 kcal mol⁻¹.

Why Does HOD Not Need a Cofactor? Finally, we answer the question, how the reaction mechanism could be influenced by the use of a cofactor in HOD, e.g., iron? In particular, we hypothesize how the catalytic mechanism of HOD would be affected by a bound cofactor. In order to understand the details of the oxygen activation in HOD and to clarify why an iron cofactor is not needed, we set up another VB curve crossing diagram (Figure 8) for a hypothetical system that uses an iron(III)-superoxo cofactor. The above reflects the active species as appeared in intradiol dioxygenases, which incidentally catalyze a very similar reaction as to that described in Scheme 1. Note that iron(II)-superoxo will give rise to the same conclusions. Thus, the iron(III)-superoxo complex (⁵R') will covalently bind the dioxygen as an end-on superoxo structure and most likely will bind the substrate as a bidentate ligand via atoms O³ and O⁴. Calculations of iron(III)-superoxo complexes of nonheme iron dioxygenases resulted in a high-spin ground state with three unpaired electrons on the metal and one on the superoxo group.³² Typically calculations on nonheme iron(III)-superoxo complexes give chemical systems with considerably lesser radical character (and more anionic charge) on the terminal oxygen atom than ³O₂, and as a result the terminal oxygen atom of the iron(III)-superoxo group will become more electrophilic. However, the terminal oxygen atom is located at a relatively large distance from carbon atom C² (approximately 4.2 Å), consequently, in the case of HOD, the substrate activation will incur a large geometrical change and therefore introducing a cofactor will not lower the barriers with respect to those found without cofactor.

Thus, in HOD the substrate *N*-heteroaromatic ring is chemically different to the aromatic ring present in the substrates of catechol dioxygenases. Then, breaking of the π -bond in HOD will require lesser energy than the breaking of the π -bond of the aromatic ring in catechol dioxygenases.

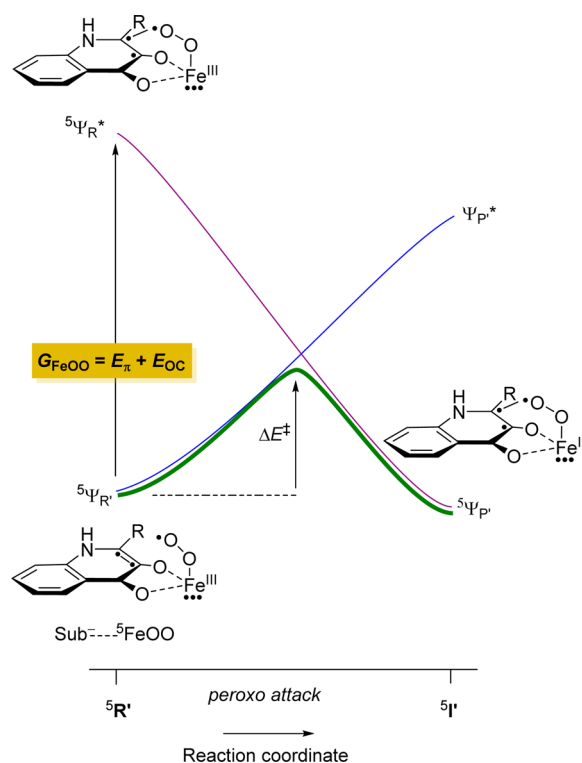


Figure 8. Valence bond curve crossing diagram for the formation of a quintet spin peroxy complex from reactants. Dots represents relevant valence electrons and lines between dots are bonds.

Furthermore, the nitrogen atom (N¹) in the MHQ ring will increase the electron density of the neighboring carbon atom (C²) and make it more susceptible for C–O bond formation with dioxygen. As such, the difference in substrate between HOD and catechol dioxygenases will require lesser energy for substrate dioxygenation, which can even be directly done with ³O₂.

As above, the height of the barrier will be a fraction of the excitation energy (G_{FeOO}) for the transition from the ground state to the excited state representing the product wave function. An analysis of the VB structures for the ground and excited states implicates that also G_{FeOO} is connected to the breaking of the π -bond between C² and C³ (E_{π}) as well as the bond formation energy for the C–O interaction (E_{CO}), eq 7.

$$G_{\text{FeOO}} = E_{\pi} + E_{\text{OC}} \quad (7)$$

Binding of MHQ to a cofactor, such as iron(III) is only going to marginally affect the π -bonding energy (E_{π}). Moreover, little changes in C–O bond formation energy are expected either as the step does not involve an electron transfer or any charge reorganization. Therefore, binding of substrate to a cofactor is not going to increase the reaction rate dramatically from an electronic perspective. Furthermore, binding of the substrate as a bidentate ligand to the iron will make the distance between the terminal oxygen atom of the iron(III)-superoxo and carbon atom C² large and will lead to an increase in barrier heights along the chemical reaction due to electrostatic interactions. Consequently, a cofactor is not beneficial for the HOD reaction process and therefore it has developed without it. Thus, the mechanism of HOD is different from, for instance, catechol intradiol dioxygenases, where the catechol-bound iron(III) complex binds molecular oxygen to form an iron(III)-superoxo.^{8,33} The latter attacks the carbonyl carbon of the

substrate to form a ring-structure analogous to I_1 reported above. This step, however, is not rate determining and the following dioxygen bond cleavage is higher in energy.^{9b} As a consequence, changes in the rate-determining step and the nature of the substrate and cofactor, will drive the reaction differently.

CONCLUSIONS

We present a combined experimental and computational study into the catalytic mechanism of MHQ dioxygenation by a cofactor-free dioxygenase. Using spectroscopic and kinetic studies we investigated substrate and substrate analogues conversion to products using wt and active site variants. These studies established key roles of a number of active site residues, namely, His₂₅₁, Asp₁₂₆, Ser₁₀₁ and Trp₁₆₀. Thus, an active site dyad of His₂₅₁/Asp₁₂₆ deprotonates the substrate, which make it susceptible for C–O bond formation and later electron transfer. The substrate is further stabilized into the binding pocket through hydrogen bonding interactions with a number of residues that hold it in the ideal orientation and assist with C–O bond formation and electron transfer pathways. Finally, computational modeling establishes what the rate-determining step in the mechanism is and how it is affected by changes to the substrate, i.e., replacing methyl by *n*-butyl, fluoride, etc. A valence bond model explains the obtained mechanisms and predicts that the addition of a cofactor to the active site will not benefit the reaction mechanism and most likely will slow the reaction down.

ASSOCIATED CONTENT

Supporting Information

Table with kinetics and computational data, as well as Schemes and Figures with kinetic, spectroscopic and computational results. We also provide Cartesian coordinates of optimized DFT structures. The Supporting Information is available free of charge on the ACS Publications website at DOI: 10.1021/jacs.5b03836.

AUTHOR INFORMATION

Corresponding Authors

*nigel.scrutton@manchester.ac.uk

*sam.devisser@manchester.ac.uk

Notes

The authors declare no competing financial interest.

ACKNOWLEDGMENTS

This research was supported by the BBSRC, which is thanked for support via grant number BB/I020543/1 (SdV & NSS), BB/I020411/1 (RAS) as well as for a DTP studentship to MGQ. The EPSRC is thanked for an Established Career Fellowship to NSS. The National service of Computational Chemistry Software (NSCCS) is thanked for additional CPU time.

REFERENCES

(1) (a) Solomon, E. I.; Brunold, T. C.; Davis, M. I.; Kemsley, J. N.; Lee, S. K.; Lehnert, N.; Neese, F.; Skulan, A. J.; Yang, Y. S.; Zhou, J. *Chem. Rev.* **2000**, *100*, 235–349. (b) Bugg, T. D. H. *Curr. Opin. Chem. Biol.* **2001**, *5*, 550–555. (c) Costas, M.; Mehn, M. P.; Jensen, M. P.; Que, L., Jr. *Chem. Rev.* **2004**, *104*, 939–986. (d) Bruijninx, P. C. A.; van Koten, G.; Klein Gebbink, R. J. M. *Chem. Soc. Rev.* **2008**, *37*, 2716–2744. (e) Bugg, T. D. H.; Ramaswamy, S. *Curr. Opin. Chem. Biol.* **2008**, *12*, 134–140. (f) Abu-Omar, M. M.; Loaiza, A.; Hontzeas,

N. Chem. Rev. **2005**, *105*, 2227–2252. (g) Kryatov, S. V.; Rybak-Akimova, E. V.; Schindler, S. *Chem. Rev.* **2005**, *105*, 2175–2226. (h) Kovaleva, E. G.; Lipscomb, J. D. *Nat. Chem. Biol.* **2008**, *4*, 186–193. (i) He, P.; Moran, G. R. *Curr. Opin. Chem. Biol.* **2009**, *13*, 443–450. (j) Ray, K.; Pfaff, F. F.; Wang, B.; Nam, W. *J. Am. Chem. Soc.* **2014**, *136*, 13942–13958. (k) Solomon, E. I.; Heppner, D. E.; Johnston, E. M.; Ginsbach, J. W.; Cirera, J.; Qayyum, M.; Kieber-Emmons, M. T.; Kjaergaard, C. H.; Hadt, R. G.; Tian, L. *Chem. Rev.* **2014**, *114*, 3659–3853. (l) Shaik, S.; Hirao, H.; Kumar, D. *Nat. Prod. Rep.* **2007**, *24*, 533–552.

(2) (a) Platten, M.; von Knebel Doeberitz, N.; Oezen, I.; Wick, W.; Ochs, K. *Front. Immunol.* **2014**, *5*, 673–673. (b) Prendergast, G. C.; Smith, C.; Thomas, S.; Mandik-Nayak, L.; Laury-Kleintop, L.; Metz, R.; Muller, A. J. *Cancer Immunol. Immunother.* **2014**, *63*, 721–735. (c) Munn, D. H.; Mellor, A. L. *Trends Immunol.* **2013**, *34*, 137–143. (d) Sikalidis, A. K. *Pathol. Oncol. Res.* **2015**, *21*, 9–17.

(3) Prescott, A. G.; John, P. *Annu. Rev. Plant. Physiol. Plant. Mol. Biol.* **1996**, *47*, 245–271.

(4) (a) Gibson, D. T.; Parales, R. E. *Curr. Opin. Biotechnol.* **2000**, *11*, 236–243. (b) Karlsson, A.; Parales, J. V.; Parales, R. E.; Gibson, D. T.; Eklund, H.; Ramaswamy, S. *Science* **2003**, *299*, 1039–1042.

(5) (a) Bugg, T. D. H. *Tetrahedron* **2003**, *59*, 7075–7101. (b) de Visser, S. P., Kumar, D., Eds.; *Iron-Containing Enzymes: Versatile Catalysts of Hydroxylation Reactions in Nature*; RCS Publishing: Cambridge, U.K., 2011. (c) Diaz, E.; Jimenez, J. I.; Nogales, J. *Curr. Opin. Biotechnol.* **2013**, *24*, 431–442. (d) Blomberg, M. R. A.; Borowski, T.; Himo, F.; Liao, R.-Z.; Siegbahn, P. E. M. *Chem. Rev.* **2014**, *114*, 3601–3658.

(6) (a) Groce, S. L.; Lipscomb, J. D. *Biochemistry* **2005**, *44*, 7175–7188. (b) Walsh, T. A.; Ballou, D. P.; Mayer, R.; Que, L., Jr. *J. Biol. Chem.* **1983**, *258*, 4422–4427.

(7) (a) Vaillancourt, F. H.; Barbosa, C. J.; Spiro, T. G.; Bolin, J. T.; Blades, M. W.; Turner, R. F. B.; Eltis, L. D. *J. Am. Chem. Soc.* **2002**, *124*, 2485–2496. (b) Davis, M. I.; Orville, A. M.; Neese, F.; Zaleski, J. M.; Lipscomb, J. D.; Solomon, E. I. *J. Am. Chem. Soc.* **2002**, *124*, 602–614.

(8) (a) Kovaleva, E. G.; Lipscomb, J. D. *Science* **2007**, *316*, 453–457. (b) Knoop, C. J.; Purpero, V. M.; Lipscomb, J. D. *Proc. Natl. Acad. Sci. U. S. A.* **2015**, *112*, 388–393.

(9) (a) Deeth, R. J.; Bugg, T. D. H. *J. Biol. Inorg. Chem.* **2003**, *8*, 409–418. (b) Borowski, T.; Siegbahn, P. E. M. *J. Am. Chem. Soc.* **2006**, *128*, 12941–12953.

(10) Fetzner, S.; Steiner, R. A. *Appl. Microbiol. Biotechnol.* **2010**, *86*, 791–804.

(11) (a) Bauer, I.; Max, N.; Fetzner, S.; Lingens, F. *Eur. J. Biochem.* **1996**, *240*, 576–583. (b) Steiner, R. A.; Janssen, H. J.; Roversi, P.; Oakley, A. J.; Fetzner, S. *Proc. Natl. Acad. Sci. U. S. A.* **2010**, *107*, 657–662. (c) Thierbach, S.; Bui, N.; Zapp, J.; Chhabra, S. R.; Kappl, R.; Fetzner, S. *Chem. Biol.* **2014**, *20*, 1–9.

(12) (a) Frerichs-Deeken, U.; Rangelova, K.; Kappl, R.; Huttermann, J.; Fetzner, S. *Biochemistry* **2004**, *43*, 14485–14499. (b) Frerichs-Deeken, U.; Fetzner, S. *Curr. Microbiol.* **2005**, *51*, 344–352. (c) Hernández-Ortega, A.; Quesne, M. G.; Bui, S.; Heuts, D.; Steiner, R. A.; Heyes, D. J.; de Visser, S. P.; Scrutton, N. S. *J. Biol. Chem.* **2014**, *289*, 8620–8632.

(13) (a) de Visser, S. P.; Quesne, M. G.; Martin, B.; Comba, P.; Ryde, U. *Chem. Commun.* **2014**, *50*, 262–282. (b) Kumar, S.; Faponle, A. S.; Barman, P.; Vardhaman, A. K.; Sastri, C. V.; Kumar, D.; de Visser, S. P. *J. Am. Chem. Soc.* **2014**, *136*, 17102–17115. (c) Vardhaman, A. K.; Barman, P.; Kumar, S.; Sastri, C. V.; Kumar, D.; de Visser, S. P. *Angew. Chem., Int. Ed.* **2013**, *52*, 12288–12292.

(14) Frisch, M. J.; et al. *Gaussian 09*, Revision C.01; Gaussian, Inc: Wallingford, CT, 2010.

(15) (a) Becke, A. D. *J. Chem. Phys.* **1993**, *98*, 1372–1377. (b) Lee, C. T.; Yang, W. T.; Parr, R. G. *Phys. Rev. B: Condens. Matter Mater. Phys.* **1988**, *37*, 785–789. (c) Ditchfield, R.; Hehre, W. J.; Pople, J. A. *J. Chem. Phys.* **1971**, *54*, 724–728. (d) McLean, A. D.; Chandler, G. S. *J. Chem. Phys.* **1980**, *72*, 5639–5648.

(16) (a) Vardhaman, A. K.; Sastri, C. V.; Kumar, D.; de Visser, S. P. *Chem. Commun.* **2011**, 47, 11044–11046. (b) Heyes, D. J.; Sakuma, M.; de Visser, S. P.; Scrutton, N. S. *J. Biol. Chem.* **2009**, 284, 3762–3767.

(17) Linstrom, P. J.; Mallard, W. G. *J. Chem. Eng. Data* **2001**, 46, 1059–1063.

(18) (a) de Visser, S. P. *Chem. Commun.* **2007**, 171–173. (b) Quesne, M. G.; Latifi, R.; Gonzalez-Ovalle, L. E.; Kumar, D.; de Visser, S. P. *Chem.—Eur. J.* **2014**, 19, 435–446.

(19) Hammett, L. P. *J. Am. Chem. Soc.* **1937**, 59, 96–103.

(20) Torres Pazmino, D. E.; Winkler, M.; Glieder, A.; Fraaije, M. W. *J. Biotechnol.* **2010**, 146, 9–24.

(21) Veldhuizen, E. J. A.; Vaillancourt, F. H.; Whiting, C. J.; Hsiao, M. M. Y.; Gingras, G.; Xiao, Y. F.; Tanguay, R. M.; Boukouvalas, J.; Eltis, L. D. *Biochem. J.* **2005**, 386, 305–314.

(22) Vaillancourt, F. H.; Han, S.; Fortin, P. D.; Bolin, J. T.; Eltis, L. D. *J. Biol. Chem.* **1998**, 273, 34887–34895.

(23) Entsch, B.; Ballou, D. P. *Biochim. Biophys. Acta* **1989**, 999, 313–322.

(24) Bull, C.; Ballou, D. P.; Otsuka, S. *J. Biol. Chem.* **1981**, 256, 2681–2686.

(25) (a) Shaik, S.; Kumar, D.; de Visser, S. P. *J. Am. Chem. Soc.* **2008**, 130, 10128–10140. (b) Sainna, M. A.; Kumar, S.; Kumar, D.; Fornarini, S.; Crestoni, M. E.; de Visser, S. P. *Chem. Sci.* **2015**, 6, 1516–1529. (c) Kumar, D.; Sastry, G. N.; de Visser, S. P. *Chem.—Eur. J.* **2011**, 17, 6196–6205. (d) Kumar, D.; Karamzadeh, B.; Sastry, G. N.; de Visser, S. P. *J. Am. Chem. Soc.* **2010**, 132, 7656–7667. (e) de Visser, S. P. *J. Am. Chem. Soc.* **2010**, 132, 1087–1097.

(26) Shaik, S. S.; Hiberty, P. C. *A Chemist's Guide to Valence Bond Theory*; John Wiley & Sons: Hoboken, NJ, 2008.

(27) (a) Nardini, M.; Dijkstra, B. W. *Curr. Opin. Struct. Biol.* **1999**, 9, 732–737. (b) Holmquist, M. *Curr. Protein Pept. Sci.* **2000**, 1, 209–235.

(28) (a) Roth, J. P.; Klinman, J. P. *Proc. Natl. Acad. Sci. U. S. A.* **2003**, 100, 62–67. (b) Gadda, G. *Biochemistry* **2012**, 51, 2662–2669. (c) Zhao, G.; Bruckner, R. C.; Jorns, M. S. *Biochemistry* **2008**, 47, 9124–9135. (d) Prabhakar, R.; Siegbahn, P. E. M.; Minaev, B. F. *Biochim. Biophys. Acta, Proteins Proteomics* **2003**, 1647, 173–178. (e) Hernández-Ortega, A.; Lucas, F.; Ferreira, P.; Medina, M.; Guallar, V.; Martínez, A. T. *Biochemistry* **2012**, 51, 6595–6608. (f) McDonald, C. A.; Fagan, R. L.; Collard, F.; Monnier, V. M.; Palfey, B. A. *J. Am. Chem. Soc.* **2011**, 133, 16809–16811.

(29) Carter, P.; Wells, J. A. *Nature* **1988**, 332, 564–568.

(30) (a) Dunn, G.; Montgomery, M. G.; Mohammed, F.; Coker, A.; Cooper, J. B.; Robertson, T.; Garcia, J. L.; Bugg, T. D. H.; Wood, S. P. *J. Mol. Biol.* **2005**, 346, 253–265. (b) Li, J.-J.; Bugg, T. D. H. *Org. Biomol. Chem.* **2007**, 5, 507–513. (c) Li, C.; Montgomery, M. G.; Mohammed, F.; Li, J. J.; Wood, S. P.; Bugg, T. D. H. *J. Mol. Biol.* **2005**, 346, 241–251.

(31) Tsukada, H.; Blow, D. M. *J. Mol. Biol.* **1985**, 184, 703–711.

(32) (a) Borowski, T.; Bassan, A.; Siegbahn, P. E. M. *Chem.—Eur. J.* **2004**, 10, 1031–1041. (b) Jastrzebski, R.; Quesne, M. G.; Weckhuysen, B. M.; de Visser, S. P.; Bruijninx, P. C. A. *Chem.—Eur. J.* **2014**, 20, 15686–15691.

(33) (a) Vaillancourt, F. H.; Bolin, J. T.; Eltis, L. D. *Crit. Rev. Biochem. Mol. Biol.* **2006**, 41, 241–267. (b) Hitomi, Y.; Yoshida, M.; Higuchi, M.; Minami, H.; Tanaka, T.; Funabiki, T. *J. Inorg. Biochem.* **2005**, 99, 755–763. (c) Bruijninx, P. C. A.; Lutz, M.; Spek, A. L.; Hagen, W. R.; van Koten, G.; Klein Gebbink, R. J. M. *Inorg. Chem.* **2007**, 46, 8391–8402. (d) Pau, M. Y. M.; Davis, M. I.; Orville, A. M.; Lipscomb, J. D.; Solomon, E. I. *J. Am. Chem. Soc.* **2007**, 129, 1944–1958. (e) Siegbahn, P. E. M.; Haeffner, F. J. *J. Am. Chem. Soc.* **2004**, 126, 8919–8932.